Verification and comparison of four numerical schemes for a 1D viscoelastic blood flow model

Xiaofei Wang, Jose-Maria Fullana, Pierre-Yves Lagrée

Verification and comparison of four numerical schemes for a 1D viscoelastic blood flow model

Xiaofei Wang*, Jose-Maria Fullana, Pierre-Yves Lagrée
CNRS & UPMC Univ Paris 06, UMR 7190,
Institut Jean Le Rond ∂'Alembert, Boîte 162, F-75005 Paris, France

February 21, 2013

Abstract

In this paper, we present four numerical schemes for a 1D viscoelastic blood flow model. In the case with a small nonlinearity (small amplitude of wave), asymptotic analysis predicts several behaviours of the wave: propagation in a uniform tube, attenuation of the amplitude due to the skin friction, diffusion due to the viscosity of the wall, and reflection and transmission at a branching point. These predictions are compared very favorably with all of the numerical solutions. The schemes are also tested in case with a larger nonlinearity. Finally, we apply all of the schemes on a relatively realistic arterial system with 55 arteries. The schemes are compared in four aspects: the spatial and temporal convergence speed, the ability to capture shock phenomena, the computation speed and the complexity of the implementation. The suitable conditions for the application of the various schemes are discussed.

Keywords: blood flow; 1D flow modelling; vascular network; numerical simulation

1 Introduction

Despite there are several computations of blood flow in realistic arteries ([4, 15]), those computations are restricted to a given segment of artery and are time and memory consuming. Hence, direct computing of the blood flow in the complete human arterial system is up to now an impossible task. One has to do very severe modeling to obtain a tractable system of equations. A common model is the 1D model obtained by taking averaged equations of the full complicated system. It has been validated by *in vitro* experimental [38, 45, 1] and *in vivo* clinical [37, 36] data. This 1D modeling of arterial blood flow is a very important

*corresponding author

approach for investigating the hemodynamics of the cardiovascular system for the several following reasons. The wave solutions are well computed and the pulse wave carries many informations about the cardiovascular system, or even the functioning of other organs. For example, the Pulse Wave Velocity (PWV) has been recognized by European Society of Hypertension as integral to the diagnosis and treatment of hypertension [26, 5]. It allows fast enough numerical computations. So, it is attractive to implement it on real-time applications for medical planning. It may also provide pertinent boundary conditions in multi-scale models by coupling 3D simulations and 1D networks [10].

The 1D governing equations can be obtained by integrating Navier-Stokes equations across the cross-section of a circular vessel with the assumption of a long wave length and axisymmetric velocity profile [21, 40, 12]. It results in a system of two partial differential equations of mass conservation and momentum conservation for the fluid. This system is in flow rate Q, cross-section A and average pressure P. It is closed by a model of arterial wall which relates the pressure and the cross-section. All the three above equations lead a final system which is nonlinear and dominated by hyperbolicity properties. Depending on the details of the model of the arterial wall, there may be a diffusive term by the viscosity of the wall or/and a dispersion term by the axial tension.

In the case with weak nonlinearity (small perturbations around the equilibrium state [23, 33]), one way to solve the 1D governing equations is to linearize them and find solutions in frequency domain [44, 31]. Although the linearized model is simplified, it still can provide relevant insights of the arterial system [44, 31]. Nevertheless, a solution for a more realistic case with a moderate nonlinearity is still needed.

Recently, several numerical schemes have been proposed and used to solve these kind of nonlinear 1D equations in time domain, roughly we classify them as :

- Finite Difference (FD) [48, 42, 37, 38, 32, 34]
- Finite Volume (FV) [46, 7, 6]
- Finite Element (FE), [39, 11, 1, 25]
- Discontinuous Galerkin (DG) (It can be seen as a kind of FE, but we list it separately for its important unique properties) [39, 1, 29, 30, 28]

All of these schemes have been successfully applied in other communities where people have to solve similar hyperbolic problems : 1D compressible Euler equations and shallow water equations. For instance, the MacComack scheme was designed for gas dynamics and it was then successfully used to compute blood flow in veins in reference [13]. Also inspired by the success of applications of FV schemes in gas dynamics and shallow water equations, Cavallini et al. [6] proposed high order non-oscillating FV schemes for blood flow and Delestre et al. [7] obtained "well balanced" schemes which properly treat the source term induced by a tapered artery.

It is clear that FD schemes are not flexible to treat complex computational geometries in high dimensions (2D or 3D). But, in 1D and low order accuracy schemes, FD, FE and FV schemes are in fact completely equivalent for linear problems. For nonlinear problems, sharp gradient solutions may appear. The performance of FD need tests in the arterial case (where non linearities are moderate). Within the framework of FE and FV, the approaches to achieve high resolution schemes are different. The solutions given by these schemes need also to be investigated in our problem. The accuracy of DG may be tuned by the order of the degree of the polynomial or by the mesh size and this is suitable for convection dominated problem. It has been used by many researchers on 1D blood flow simulation. Thus it is also included in this paper for comparisons with other schemes. Moreover, in the literature, there are few references on the numerical treatment of the viscosity of the arterial wall ([36]). We propose an operator splitting (in the FD, FV and FE frameworks) to treat the parabolic behaviour of the wall viscosity. In the DG setting, we apply a local discontinuous Galerkin method for diffusive flux.

In this paper, we present in Section (2) the governing equations and in Section (3) the numerical details. In Section (3) we first discuss the treatment of the boundary conditions and then the discretization. We apply four schemes in various frameworks: MacCormack, second order finite volume, Taylor-Galerkin, and discontinuous Galerkin. We deliberately give many details, because those methods are scattered in different literatures. In Section (4), we consider the main behaviours of pulse wave: the attenuation due to the skin friction, the diffusion due to the viscosity of the wall, the transmissions and reflections at a branching point and the wavefront steepening phenomena due to convections. The numerical solutions are verified with the analytical predictions. Finally we compute a full network of 55 arteries. In these settings, we compare the performances of the various methods.

2 The 1D model of arterial blood flow

2.1 1D mathematical model

Under the assumption of an axisymmetric velocity profile, the 1D arterial blood flow model can be written as:

$$\frac{\partial A}{\partial t} + \frac{\partial Q}{\partial x} = 0, \tag{1}$$

$$\frac{\partial Q}{\partial t} + \frac{\partial}{\partial x}(\alpha \frac{Q^2}{A}) + \frac{A}{\rho}\frac{\partial P}{\partial x} = -C_f \frac{Q}{A}, \tag{2}$$

where as stated above, A is the cross-sectional area of the artery, Q the flow rate or flux, and ρ the density of blood. The factor α is the momentum correction factor, and C_f is the skin friction coefficient. They depend on the shape of the velocity profile. Usually, the profile can be estimated from the Womersley number which is defined as $R\sqrt{\omega/\nu}$, with R the radius of the vessel, ω the

frequency of the pulse wave and ν the kinematic viscosity of the fluid. With a small Womersley number, we can take a Poiseuille (parabolic) profile. In that case $\alpha = \frac{4}{3}$ and $C_f = 8\pi\nu$. This choice is only valid for very viscous flows (see [21, 20]). In practice, viscosity is not so large, and the profile is more flat. For a completely flat profile α equals 1. This value is often used since it leads to a considerable simplification in analysis and the loss of relevance of the model is very small in most cases [11]. Thus we assume its value is 1 in this paper. The value of C_f also depends on the velocity profile and it has significant influence on the pulse wave. In practical applications, its value has to be determined according to the particular problem at hand (both *in vitro* and *in vivo*). We assume its value is $8\pi\nu$ according to the Poiseuille profile (but we know that it is a crude approximation). As our purpose is numerical comparisons, we do not discuss more the influence of α and C_f.

To close the system, several viscoelastic constitutive relations for arteries have been presented in some papers, like [2, 1, 35]. Among them, we use the Kelvin-Voigt model which is the most simple. We assume that the arterial wall is thin, isotropic, homogeneous, incompressible, and moreover that it deforms axisymmetrically with each circular cross-section independently of the others. We denote the undeformed section by A_0 and the exterior pressure of the vessel by P_{ext}. Then, the final relation linking A and P is the Kelvin-Voigt model:

$$P = P_{ext} + \beta(\sqrt{A} - \sqrt{A_0}) + \nu_s \frac{\partial A}{\partial t}, \tag{3}$$

with the stiffness coefficient β,

$$\beta = \frac{\sqrt{\pi} E h}{(1-\eta^2) A_0},$$

and the viscosity coefficient ν_s,

$$\nu_s = \frac{\sqrt{\pi}\phi h}{2(1-\eta^2) A_0 \sqrt{A}}, \tag{4}$$

where η is the Poisson ration, which is 0.5 for an incompressible material, E is the Young's modulus, h is the thickness of the wall and ϕ the wall viscosity. For convenience, we will define $C_v = \frac{A_0 \nu_s}{\rho}$ thereafter. We note that in absence of wall viscosity we retrieve the classical Hooke's law.

2.2 Characteristic structure of the system

After having defined the system of equations, we remind its hyperbolic nature in writing it in characteristic form. This discussion is classical, and may be found in text books ([12, 22]) The notations we introduce here will be useful for the discussion of the numerical solvers. We may assume P_{ext} is constant along the axial variable x, and substitute the constitutive relation 3 into Eq. 2. We note that $\frac{\partial A}{\partial t}$ can be replaced by $-\frac{\partial Q}{\partial x}$ thanks to Eq. 1. The equation for the balance

of momentum turns out

$$\frac{\partial Q}{\partial t} + \frac{\partial}{\partial x}\left(\frac{Q^2}{A} + \frac{\beta}{3\rho}A^{\frac{3}{2}}\right) - \frac{A}{\rho}\frac{\partial}{\partial x}\left(\nu\frac{\partial Q}{\partial x}\right) = -C_f\frac{Q}{A} + \frac{A}{\rho}\left(\partial_x(\beta\sqrt{A_0}) - \frac{2}{3}\sqrt{A}\partial_x\beta\right). \tag{5}$$

Under the assumption of a small perturbation of A, we approximate the term $\frac{A}{\rho}\frac{\partial}{\partial x}(\nu\frac{\partial Q}{\partial x})$ by $C_v\frac{\partial^2 Q}{\partial x^2}$ with the already presented coefficient $C_v = \frac{A_0\nu_s}{\rho}$. The governing equations may be written as:

$$\frac{\partial U}{\partial t} + \frac{\partial F}{\partial x} = S, \tag{6}$$

where

$$U = \begin{pmatrix} A \\ Q \end{pmatrix} \quad F = F_c + F_v = \begin{pmatrix} Q \\ \frac{Q^2}{A} + \frac{\beta}{3\rho}A^{\frac{3}{2}} \end{pmatrix} + \begin{pmatrix} 0 \\ -C_v\frac{\partial Q}{\partial x} \end{pmatrix}$$

and

$$S = \begin{pmatrix} 0 \\ -C_f\frac{Q}{A} + \frac{A}{\rho}\left(\partial_x(\beta\sqrt{A_0}) - \frac{2}{3}\sqrt{A}\partial_x\beta\right) \end{pmatrix}.$$

U is the conservative variable, F the corresponding fluxes and S the source term. Note that the flux (scaled by constant density) consists in two parts, the convective F_c and the diffusive F_v. We recognize $\frac{Q^2}{A}$ due to the fluid flow, $\frac{\beta}{3\rho}A^{\frac{3}{2}}$ due to the elasticity, and $C_v\frac{\partial Q}{\partial x}$ due to the viscosity of the wall. In general, the suitable numerical techniques for the convective and diffusive flux are different. Thus it is common to separate the diffusive term and put it on the right side. Thus we may write the problem in convection-diffusion form:

$$\frac{\partial U}{\partial t} + \frac{\partial F}{\partial x} = S + D \tag{7}$$

with

$$F = F_c, \quad D = \begin{pmatrix} 0 \\ C_v\frac{\partial^2 Q}{\partial x^2} \end{pmatrix}.$$

Temporarily, we consider the homogeneous part and consider non-homogeneous part later. Expanding the derivative of the flux, the homogeneous part can be written in a quasi-linear form

$$\frac{\partial U}{\partial t} + J_c\frac{\partial U}{\partial x} = 0 \tag{8}$$

where J_c is the Jacobian matrix

$$J_c = \begin{pmatrix} 0 & 1 \\ \frac{Q^2}{A^2} + c^2 & 2\frac{Q}{A} \end{pmatrix}$$

with the Moens-Korteweg celerity

$$c = \sqrt{\frac{\beta}{2\rho}A^{\frac{1}{2}}}. \tag{9}$$

In reality, A is always positive, therefore c is real. It is the speed of the pressure wave with respect to the fluid flow. The matrix J_c has two different eigenvalues

$$\lambda_{1,2} = \frac{Q}{A} \pm c. \tag{10}$$

Linear algebra shows J_c must be diagonalizable in the form $J_c = R\Lambda R^{-1}$. The columns of R are the right eigenvectors of J_c. Left multiplying Eq. 8 by R^{-1}, one obtains

$$R^{-1}\frac{\partial U}{\partial t} + R^{-1}R\Lambda R^{-1}\frac{\partial U}{\partial x} = 0.$$

By introducing a new unknown variable vector which satisfies $\partial_U W = R^{-1}$, the previous equation can be transformed into

$$\frac{\partial W}{\partial t} + \Lambda\frac{\partial W}{\partial x} = 0. \tag{11}$$

$W_{1,2}$ can be readily obtained by integrating $\partial_U W = R^{-1}$ componentwise

$$W_{1,2} = \frac{Q}{A} \pm 4c. \tag{12}$$

$W = [W_1, W_2]^T$ is called Riemann invariant vector or characteristics. In time-space, $W_{1,2}$ are constants along the lines $D_t X_{1,2}(t) = \lambda_{1,2}$. In physiological conditions, $\lambda_1 > 0 > \lambda_2$. The two families of characterisic propagate in opposite directions. The homogeneous part is a subcritical hyperbolic system. For further use, we get the expression for A and Q by inverting the relation 12,

$$A = \frac{(W_1 - W_2)^4}{1024}\left(\frac{\rho}{\beta}\right)^2, \quad Q = A\frac{W_1 + W_2}{2}. \tag{13}$$

In the non-homogeneous part, the skin friction term dissipates the momentum and the second order derivative of Q is diffusive. In physiological conditions, the Womersley number is not too big and the artery is almost uniform, the source term will be very small. These phenomena are dominated by the convection terms. If the properties of the artery have sharp variations, we will deal with this problem by treating the artery as two different connected segments.

3 Numerical solvers

Having defined the problem and notations, in this section we present the numerical solvers. The original problem is split into two subproblems, hyperbolic and parabolic. Three numerical schemes are presented to treat the hyperbolic subproblem. For the parabolic subproblem, Crank-Nicolson method is suitable. Because of the duplication of values at the interface of elements in the DG scheme setting, there are difficulties to apply Crank-Nicolson scheme. A local discontinuous Galerkin method is adopted to treat the original advection-diffussion problem.

3.1 Operator splitting

There are explicit high resolution schemes for hyperbolic problems. But for parabolic problem, implicit schemes are necessary in general for a reasonable time step for time integration. Thus we applied a fractional step or operator splitting method for the problem. The original problem Eq. (7) is split into to a hyperbolic subproblem,

$$\frac{\partial U}{\partial t} + \frac{\partial F}{\partial x} = S \tag{14}$$

and a parabolic one,

$$\frac{\partial U}{\partial t} = D. \tag{15}$$

Let's consider the time intervals (t^n, t^{n+1}), for $n = 0, 1, ...$, with $t^n = n\Delta t$. In every time interval, the hyperbolic problem is solved to get a predictor U^*, which is used as the initial condition (I.C.) of the second problem. The second step can be viewed as a corrector. The original problem is approximated by a sequential application of the two subproblems in a certain order.

From data U^n, we may make a prediction U^* by evolving time Δt of the hyperbolic subproblem, and correct it with the evolution over Δt of the parabolic subproblem,

$$U^n \xrightarrow{e^{\Delta t\mathcal{H}}} U^* \xrightarrow{e^{\Delta t\mathcal{P}}} U^{n+1}. \tag{16}$$

$e^{\Delta t\mathcal{H}}$ means to solve the hyperbolic subproblem over Δt. $e^{\Delta t\mathcal{P}}$ has the same meaning for the parabolic subproblem. This method is called Godunov splitting. If the two subproblems are not commutable, the splitting error is $\mathcal{O}(\Delta t)$, see Chapter 17 of reference [22].

There is a 3 stage splitting called Strang splitting, which has a leading error term $\mathcal{O}(\Delta t^2)$,

$$U^n \xrightarrow{e^{\frac{1}{2}\Delta t\mathcal{P}}} U^* \xrightarrow{e^{\Delta t\mathcal{H}}} U^{**} \xrightarrow{e^{\frac{1}{2}\Delta t\mathcal{P}}} U^{n+1}. \tag{17}$$

We will see in the section about diffusion that in reality the errors induced by the two splittings are very close. That is because the coefficient of the term $\mathcal{O}(\Delta t)$ is much smaller then the coefficient of $\mathcal{O}(\Delta t^2)$. Thus, usually Godunov splitting is sufficient.

Because the original problem is dominated by the hyperbolic part, the system must be driven mainly by the Boundary Conditions (B.C.) through the first subproblem. Thus we discuss the B.C. of the hyperbolic part in the next subsection and present the treatment of B.C. for the parabolic part in section (3.6) together with the numerical solvers.

3.2 Initial and boundary conditions

3.2.1 Initial conditions

Assume we are interested in the blood flow in an arterial segment $(0, L)$ within a time interval $(0, T)$. For a convection-diffusion problem, the PDE should be complemented by an I.C. and two B.C. In reality, the blood flow should achieve

a steady periodic pattern after a certain interval of time, which is not influenced by the I.C. Thus, the I.C. can be set arbitrarily, say, $U(t=0,x)=(A_0,0)$, for convenience.

3.2.2 Inlet and outlet of the hyperbolic part

Let's look back to the vector Eq. (11) again. The two components of this system are

$$\frac{\partial W_1}{\partial t}+\lambda_1\frac{\partial W_1}{\partial x}(U)=0, \tag{18}$$

$$\frac{\partial W_2}{\partial t}+\lambda_2\frac{\partial W_2}{\partial x}(U)=0, \tag{19}$$

where l_1 is the first column vector of matrix R^{-1}, which is the left eigenvector of J_c corresponding to λ_1 (the same holds for l_2). Since the two eigenvalues have opposite signs, there is exactly one incoming characteristic at each end of the computational domain. The incoming characteristic carries information from outside the domain and thus is essential to guarantee the problem to be well-posed. That is to say, the B.C. must have the form

$$W_1(0,t)=g_1(t),\quad W_2(L,t)=g_2(t), t>0.$$

The outgoing characteristic carries information from inside the domain, which can be given by the differential equations. Since $W_{1,2}$ are constants along the lines $D_tX_{1,2}(t)=\lambda_{1,2}$ in time-space plane, we can get $W_2^{n+1}(0)$ and $W_1^{n+1}(L)$ by interpolation in the data of the current time step:

$$W_2^{n+1}(0)=W_1^n\big(-\lambda_1^n(0)\Delta t\big),\quad W_1^{n+1}(L)=W_2^n\big(L-\lambda_2^n(L)\Delta t\big). \tag{20}$$

The characteristics are transformed to physical variables by the relation 13.

In reality, we rarely have the explicit expression of incoming characteristics. Usually, we want to impose physical boundary conditions, A or Q. At the inlet, if $A(t)$ is given, one can use the relation (12) to deduce:

$$W_1^{n+1}=W_2^{n+1}+8\sqrt{\frac{\beta}{2\rho}A(t)^{1/2}}.$$

If $Q(t)$ is given, similarly we obtain an approximation

$$W_1^{n+1}=-W_2^{n+1}+2\frac{Q^{n+1}}{A(0)}.$$

If $P(t)$ is given, from the wall relation (3) simplified with no viscous effect ($C_v=0$), we in fact impose:

$$W_1^{n+1}=W_2^{n+1}+8\sqrt{\frac{1}{2\rho}(P(t)+\beta A_0^{1/2})}.$$

At the outlet, some partition of the perturbation of outgoing characteristic W_1 may be reflected,

$$W_2^{n+1} = W_2^0 - R_t(W_1^{n+1} - W_1^0)$$

where R_t is the coefficient of reflection. If $R_t = 0$, the B.C. is nonreflecting. That means that the outgoing characteristic goes out without leaving any effect and that the incoming characteristic is a constant in time. If $R_t \neq 0$, that means some part of the outgoing characteristic is reflected by the resistance in the downstream arteries.

3.2.3 Conjunction points

There are many cases when conjunction points need to be considered: when there are changes of topology, sharp changes in geometry or properties. Topological change correspond to the large amount of bifurcations and some trifurcations in the arterial network. Sharp changes correspond to the sharp variation of the properties of the vessel wall, e.g. sharp increase of stiffness K due to stenting or A_0 due to aneurysm. As such derivative in the source term cause a singularity, the vessel can be treated as two segments conjuncted together.

Since all of the conjunctions can be treated with the same method, we consider a branching point as a sample problem : a main vessel with two daughter arteries. At the branching point, there are then six boundary conditions, A_p^{n+1} and Q_p^{n+1} for the outlet of the parent artery and $A_{d_1}^{n+1}$, $Q_{d_1}^{n+1}$,$A_{d_2}^{n+1}$ and $Q_{d_2}^{n+1}$ for the inlets of the two daughter arteries. From the physical point of view, the scheme has to preserve the conservation of mass flux

$$Q_p^{n+1} - Q_{d_1}^{n+1} - Q_{d_2}^{n+1} = 0 \tag{21}$$

and conservation of momentum flux

$$\frac{1}{2}\rho(\frac{Q_p^{n+1}}{A_p^{n+1}})^2 + P_p^{n+1} - \frac{1}{2}\rho(\frac{Q_{d_i}^{n+1}}{A_{d_i}^{n+1}})^2 - P_{d_i}^{n+1} = 0 \quad i = 1, 2. \tag{22}$$

P_p^{n+1} and $P_{d_i}^{n+1}$ are given by the constitutive relation for pressure (3). Moreover, the outgoing characteristics in each artery can be determined by the interpolation formula (20). $(W_1)_p^{n+1}$, given by the interpolation on the $n-th$ step data of the parent vessel, must be equal to $W_1(U_p^{n+1})$, which is given by relation (12)

$$(W_1)_p^{n+1} - W_1(U_p^{n+1}) = 0. \tag{23}$$

The same holds for W_2 on the two daughter arteries.

$$(W_2)_{d_i}^{n+1} - W_2(U_{d_i}^{n+1}) = 0 \quad i = 1, 2. \tag{24}$$

Combining Eq.s (21), (22), (23) and (24), there are 6 Eq.s with 6 unknowns. This nonlinear algebraic system can be readily solved by Newton iterative method or some other nonlinear algebraic solvers with U^n as the initial guess. We now focus on the schemes themselves, all what we presented up to now being almost common to all the schemes.

3.3 MacCormack scheme

The classical MacCormack method [24] has been developed for hyperbolic systems of conservation laws. It is a two-step predictor-corrector technique, with the following characteristics: three-point spatial stencil and two time levels (the predictor and the corrector), second-order accurate in time and space.

For the conservative system of Eq. (14) an approximate solution U^* is obtained in the first step and then corrected in the second to give the solution at time $t + \Delta t$, U^{n+1}. The numerical solution is performed in a fixed grid of $N+1$ points along the vessel axis of length L which defines the spatial resolution $\Delta x = \frac{L}{N}$, see Figure (1). The finite difference equations (at the interior grid points) are then :

1. predictor step

$$U_i^* = U_i^n - \frac{\Delta t}{\Delta x}(F_{i+1}^n - F_i^n) + \Delta t S_i^n, \quad i = 2, ...N$$

2. corrector step

$$U_i^{n+1} = \frac{1}{2}(U_i^n + U_i^*) - \frac{\Delta t}{2\Delta x}(F_i^* - F_{i-1}^*) + \frac{\Delta t}{2} S_i^*, \quad i = 2, ...N$$

F^* and S^* are evaluated with the predicted solution U^*, $F(U^*)$ and $S(U^*)$. The grid points $i = 1$ and $i = N + 1$ represent the boundary conditions.

The MacCormack scheme of integration for hyperbolic equations was in occurrence used on unsteady flow on a model of pulmonary airways [17] and compared with a classical Lax-Wendroff scheme in reference [8]. One conclusion was that both schemes show an excellent convergence for analytical steady-state solution but they are hardly applied to flows with undamped oscillations as flow near to singularities.

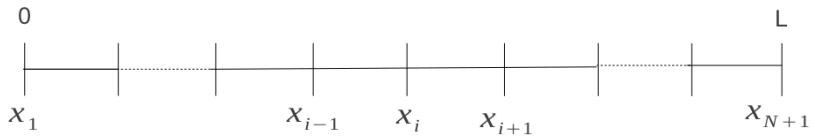

Figure 1: mesh for FD and FE

3.4 Taylor-Galerkin scheme

In this section we followed Formaggia and Sherwin's presentation for the Taylor-Galerkin scheme [39, 11, 12]. Other forms are also possible, see, for example [43]. The Taylor series for U^{n+1} up to second order is

$$U^{n+1} = U^n + \Delta t \frac{\partial U^n}{\partial t} + \frac{\Delta t^2}{2} \frac{\partial^2 U^n}{\partial t^2} + \mathcal{O}(\Delta t^3). \tag{25}$$

From Eq. (14), one obtains,

$$\frac{\partial U^n}{\partial t} = S^n - \frac{\partial F^n}{\partial x}. \tag{26}$$

Differentiation both sides with respect to t and change the order of spatial and temporal differentiation in the second term gives,

$$\frac{\partial^2 U^n}{\partial t^2} = \Big(S_U \frac{\partial U}{\partial t}\Big)^n - \frac{\partial}{\partial x}\Big(H \frac{\partial U}{\partial t}\Big)^n \tag{27}$$

where $S_U = \frac{\partial S}{\partial U}$ and $H = \frac{\partial F}{\partial U}$. Substituting Eq. (26) into Eq. (27) and then both of them into Eq. (25), one gets,

$$\begin{aligned} U^{n+1} = U^n - \Delta t \frac{\partial}{\partial x}\big[F^n + \frac{\Delta t}{2} H^n S^n\big] - \frac{\Delta t^2}{2}\big[S_U^n \frac{\partial F^n}{\partial x} - \frac{\partial}{\partial x}\big(H^n \frac{\partial F^n}{\partial x}\big)\big] \\ + \Delta t\big(S^n + \frac{\Delta t}{2} S_U^n S^n\big). \end{aligned} \tag{28}$$

For convenience, we adopt the notation

$$F_{LW}(U) = F(U) + \frac{\Delta t}{2} H(U) S(U),$$
$$S_{LW}(U) = S(U) + \frac{\Delta t}{2} S_U(U) S(U).$$

The piecewise linear function space is given as,

$$V_h^0 = \{[v_h]^2 | v_h \in \mathcal{C}^0, v_h|_{[x_i, x_{i+1}]} \in \mathcal{C}^1, v_h(0) = v_h(L) = 0, i = 1...N\}.$$

The shape function in this space has the property $\psi_i(x_j) = \delta_{ij}$, where δ_{ij} is Kronecker delta. This is both the trial function space and test function space in the Galerkin scheme. U was approximated by $U_h \in V_h^0$. We further define the inner product

$$(u, v) = \int_0^L uv dx.$$

Replace U by U_h in Eq.28, multiply both sides by basis test functions, and integrate over the domain$[0, L]$, finally we get

$$\begin{aligned} (U_h^{n+1}, \psi_i) = (U_h^n, \psi_i) + \Delta t\big(F_{LW}(U_h^n), \frac{d\psi_i}{dx}\big) - \frac{\Delta t^2}{2}\big(S_U(U_h^n)\frac{\partial F}{\partial x}(U_h^n), \psi_i\big) \\ - \frac{\Delta t^2}{2}\big(H(U_h^n)\frac{\partial F}{\partial x}(U_h^n), \frac{d\psi_i}{dx}\big) + \Delta t(S_{LW}(U_h^n), \psi_i) \quad i = 2, ...N. \end{aligned} \tag{29}$$

U^{n+1} and U^n are expanded as $U_h = \sum_{j=2}^{j=N} U_j \psi_j$. F,F_{LW},S_{LW} and H are expanded by a group finite element method instead of evaluating them directly as nonlinear functions of U_h^n. That is, for example,

$$F(U_h^n) = \sum_{j=2}^{j=N} F_j^n \psi_i,$$

where $F_i^n = F(U_i^n)$. Finally, the matrix form of the FE scheme writes

$$\mathcal{M}U^{n+1} = \mathcal{M}U^n + \Delta t \mathcal{K}^T F_{LW}^n + \Delta t \mathcal{M} S_{LW}^n - \frac{\Delta t^2}{2}\tilde{\mathcal{M}}F^n - \frac{\Delta t^2}{2}\tilde{\mathcal{K}}F^n, \quad (30)$$

where

$$\mathcal{M}_{ij} = (\psi_i, \psi_j), \quad \mathcal{K}_{ij} = (\psi_i, \frac{\partial \psi_j}{\partial x})$$

and

$$\tilde{\mathcal{M}}_{ij}(S_u) = \Big(\sum_k (S_u)_k \psi_k \frac{\partial \psi_i}{\partial x}, \psi_j\Big), \quad \tilde{\mathcal{K}}_{ij}(H) = \Big(\sum_k H_k \psi_k \frac{\partial \psi_i}{\partial x}, \frac{\psi_j}{\partial x}\Big).$$

Note that $\tilde{\mathcal{M}}$ and $\tilde{\mathcal{K}}$ are functions of S_u and H, therefore they must be updated in every time step. Also note that if the Taylor series were truncated up to the first order, and P_1 element were adopted for the spatial discretization, the scheme will be equivalent to a forward Euler combined with central difference scheme, which is unconditionally unstable for a convection problem.

3.5 Second order finite volume scheme

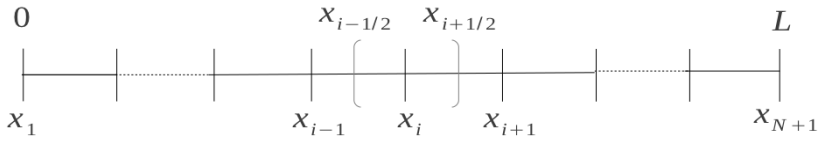

Figure 2: mesh for FV

For finite volume method, the domain is decomposed into finite volumes or cells with vertex x_i as the center of cell $[x_{i-1/2}, x_{i+1/2}]$, see Figure (2). For every cell, the conservation law must holds,

$$\int_{x_{i-1/2}}^{x_{i+1/2}} \frac{\partial U}{\partial t} dx + \int_{x_{i-1/2}}^{x_{i+1/2}} \frac{\partial F}{\partial x} dx = \int_{x_{i-1/2}}^{x_{i+1/2}} S dx. \quad (31)$$

Application of Gauss's law on the second term gives

$$\int_{x_{i-1/2}}^{x_{i+1/2}} \frac{\partial U}{\partial t} dx + F|_{x_{i+1/2}} - F|_{x_{i-1/2}} = \int_{x_{i-1/2}}^{x_{i+1/2}} S dx. \quad (32)$$

In the cells, average values are considered,

$$U_i = \frac{1}{\Delta x}\int_{x_{i-1/2}}^{x_{i+1/2}} U(x) dx, \quad S_i = \frac{1}{\Delta x}\int_{x_{i-1/2}}^{x_{i+1/2}} S(x) dx.$$

Thus Eq. 32 turns into an ordinary differential equation

$$\frac{dU_i}{dt} = -\frac{(F|_{x_{i+1/2}} - F|_{x_{i-1/2}})}{\Delta x} + S_i. \quad (33)$$

The flux at the interface of the cells have to be determined. But in general, the values of U at the two sides of the interface, U_L to the left and U_R to the right, are not equal. A unique value, called numerical flux F^*, has to be designed as a function of these two values. It is clear that a central numerical flux, $(F(U_L) + F(U_R))/2$, will lead to instabilities for a convection problem. A numerical diffusive term has to be added to stabilize the method. Many such kind of numerical flux have been proposed, for example Rusanov (or called local Lax-Friedrichs)flux. It writes

$$\mathcal{F}(U_L, U_R) = \frac{F(U_L) + F(U_R)}{2} - c\frac{U_R - U_L}{2},$$

with

$$c = \sup_{U=U_L,U_R} (\sup_{j\in 1,2} |\lambda_j(U)|)$$

where $\lambda_1(U)$ and $\lambda_2(U)$ are the eigenvalues of J_c. Other methods with less numerical diffusions, such as HLL flux, are available. Since Rusanov's method is very simple and efficient, it was adopted in this paper. If U_L and U_R equal the average values at the cell, the numerical flux will be of first order accuracy. Linear reconstructions of U within the cells are necessary for a second order numerical flux. The slope of a scalar s within the i-th cell Ds_i can be approximated as $(s_i - s_{i-1})/\Delta x$, $(s_{i+1} - s_i)/\Delta x$ or $(s_{i+1} - s_{i-1})/2\Delta x$. Then the values of s at the interfaces associated with this cell can be recovered as

$$s_{i-1/2+} = s_i - \frac{\Delta x}{2} Ds_i \text{ and } s_{i+1/2-} = s_i + \frac{\Delta x}{2} Ds_i.$$

The discretization of derivative in space can achieve a second order accuracy by this method. But the solution will have nonphysical oscillations. Some examples of oscillations induced by these methods can be found in Chapter 6 of reference [22]. Slope or flux limiter and non-oscillatory solution are integral characteristics of FV schemes. One simple slope limiter is defined as

$$\text{minmod(x,y)} = \begin{cases} \min(\text{x,y}) & \text{if } x, y \geq 0, \\ \max(\text{x,y}) & \text{if } x, y \leq 0, \\ 0 & \text{else} \end{cases}$$

Then the slope Ds_i is modified as

$$Ds_i = \text{minmod}(\frac{s_i - s_{i-1}}{\Delta x}, \frac{s_{i+1} - s_i}{\Delta x}).$$

The values of A and Q at the interfaces can be obtained as

$$A_{i-1/2+} = A_i - \frac{\Delta x}{2} DA_i, \quad A_{i+1/2-} = A_i + \frac{\Delta x}{2} DA_i$$

and

$$Q_{i-1/2+} = Q_i - \frac{\Delta x}{2} DQ_i, \quad Q_{i+1/2-} = Q_i + \frac{\Delta x}{2} DQ_i.$$

It is easy to verify that the variables are conserved by this reconstruction

$$\frac{R_{i-1/2+} + R_{i+1/2-}}{2} = R_i, \quad \frac{Q_{i-1/2+} + Q_{i+1/2-}}{2} = Q_i.$$

The adopted numerical integration in time was also of second order accuracy. Let's rewrite Eq. 33 as

$$\frac{dU}{dt} = \Phi(U)$$

where

$$\Phi(U) = -\frac{(\mathcal{F}_{i+1/2L} - \mathcal{F}_{i-1/2R})}{\Delta x} + S.$$

The flux have been replaced by numerical flux. A 2-step second order Adams-Bashforth (A-B) scheme can be applied,

$$U^{n+1} = U^n + \Delta t\big(\frac{3}{2}\Phi(U^n) - \frac{1}{2}\Phi(U^{n-1})\big).$$

This scheme can be initiated by a forward Euler method. A second order Runge-Kutta (R-K) method is also possible. But the R-K method requires one more time resolution of $\Phi(U)$ at every step. This may be offset by a larger time step allowed by the R-K method. But note also the boundary conditions are determined dynamically. The A-B method allows less resolutions of the nonlinear algebraic equations at conjunctions points. Thus we choose the A-B method for the time integration.

3.6 Treatment of the parabolic subproblem

For the previous 3 schemes, only the hyperbolic subproblem resulted from splitting was solved. Crank-Nicolson method is very suitable for the parabolic subproblem. The temporal and spatial discretization has the form,

$$\frac{U_i^{n+1} - U_i^*}{\Delta t} = \frac{C_v}{2}\big(\frac{U_{i+1}^{n+1} - 2U_i^{n+1} + U_{i-1}^{n+1}}{\Delta x^2} + \frac{U_{i+1}^* - 2U_i^* + U_{i-1}^*}{\Delta x^2}\big).$$

U^* is the solution of the first hyperbolic subproblem. The matrix of the resulting algebraic system is tridiagonal, which is quite cheap to invert. This scheme is second order accurate both on time and space. Moreover, it is unconditionally stable. It is natural to set a homogeneous Neumann B.C. for the parabolic subproblem, $\partial_x U_p(0,t) = \partial_x U_p(L,t) = 0$. The subscript p stands for the step of the parabolic subproblem.

3.7 Local Discontinuous Galerkin scheme

In FV schemes, the recovery of U_L and U_R of higher accuracy requires bigger stencil. In higher dimensions, this kind of reconstruction leads to big difficulties. On the other hand, it is quite straightforward to increase the order of approximation polynomials in one finite element. Unlike the global FE, the neighboring

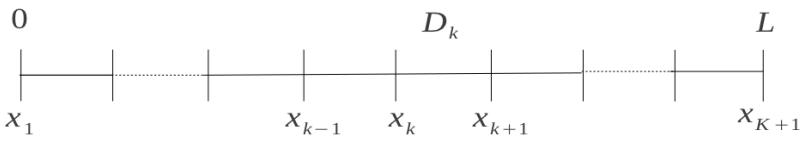

Figure 3: mesh for DG

elements do not share the same values at the interface. Numerical flux are obtained from these values, where the dynamics of the system can be considered. In DG setting, the scheme can achieve high p-accuracy for convection dominated problems. Following Hesthaven and Warburton's book [16], we present a nodal DG scheme here. The domain is decomposed into K non-overlapping elements, see Figure (3). At each element, the local approximation to the solution is a polynomial of order $N = N_p - 1$. The global approximation to U is direct summation of these local solutions:

$$U_h = \bigoplus_{k=1}^{k=K} U_h^k. \tag{34}$$

Similarly, the flux F and the source S can also be approximated by direct summation of piecewise N-th-order polynomials. The local form of the conservation law on the k-th element has the form,

$$\frac{\partial U_h^k}{\partial t} + \frac{\partial F_h^k}{\partial x} = S_h^k. \tag{35}$$

Multiplication by a test function ϕ^k at both sides of Eq. (35), and integration over one element gives

$$\left(\frac{\partial U_h^k}{\partial t}, \phi^k\right)_{D_k} + \left(\frac{\partial F_h^k}{\partial x}, \phi^k\right)_{D_k} = \left(S_h^k, \phi^k\right)_{D_k}. \tag{36}$$

Applying integration by part on the second term, we have:

$$\left(\frac{\partial U_h^k}{\partial t}, \phi^k\right)_{D_k} - \left(F_h^k, \frac{\partial \phi^k}{\partial x}\right)_{D_k} + F_h^k \phi^k \Big|_{x_k}^{x_{k+1}} = \left(S_h^k, \phi^k\right)_{D_k}. \tag{37}$$

Again, since the value of U_h at the two sides of the interface, $U_h^k(x_k)$ and $U_h^{k+1}(x_k)$, are not equal, a numerical flux F^* is introduced here. Through the numerical flux, information is communicated between elements. In practice, the second term is integrated by part again for convenience of computation. Thus we have

$$\left(\frac{\partial U_h^k}{\partial t}, \phi^k\right)_{D_k} + \left(\frac{\partial F_h^k}{\partial x}, \phi^k\right)_{D_k} + (-F_h^k \phi^k + \mathcal{F}\phi^k) \Big|_{x_k}^{x_{k+1}} = \left(S_h^k, \phi^k\right)_{D_k}. \tag{38}$$

We introduce N_p nodes within the element D_k. The local solution is expanded as

$$U_h^k(x,t) = \sum_{i=1}^{N_p} U_h^k(x_i^k,t) l_i^k(x), \tag{39}$$

where $l_i^k(x)$ is the Lagrange interpolant associated with the $i-th$ point. For the Galerkin scheme, Eq. (38)must holds for every test function $l_i^k(x)$. Thus we have N_p equations for N_p unknowns. In matrix form, the system can be written as,

$$\mathcal{M}^k \frac{dU_k}{dt} + \mathcal{K}^k F^k + (-F^k l^k + F^* l^k)\Big|_{x_k}^{x_{k+1}} = \mathcal{M}^k S^k, \tag{40}$$

where

$$\mathcal{M}^k = \left(l_i^k, l_j^k\right)_{D_k}, \quad \mathcal{K}^k = \left(\frac{dl_i^k}{dx}, l_j^k\right)_{D_k}.$$

The system of equations can be turned into a semi-discrete form,

$$\frac{dU_k}{dt} = -\mathcal{D}^k F^k - (\mathcal{M}^k)^{-1}(-F^k l^k + F^* l^k)\Big|_{x_k}^{x_{k+1}} + S^k. \tag{41}$$

where

$$\mathcal{D}_{(i,j)}^k = (\mathcal{M}^k)^{-1}\mathcal{K}_{(i,j)}^k = \left.\frac{dl_j^k}{dr}\right|_{r_i}$$

is the local differentiation operator [16]. The computation of $\mathcal{M}^k$ and $\mathcal{D}^k$ is crucial. We define an affine mapping from a reference element $(-1,1)$ to D_k,

$$x(r) = x_k + \frac{1+r}{2}(x_{k+1} - x_k).$$

The local operators can be readily computed as,

$$\mathcal{M}^k = \mathcal{J}_k \int_{-1}^{1} l_i l_j dr, \quad \mathcal{D}^k = \mathcal{J}_k \left.\frac{dl_j}{dr}\right|_{r_i},$$

where $\mathcal{J}_k = (x_{k+1} - x_k)/2$ and l_i is the Lagrange interpolation at the reference element. $\int_{-1}^{1} l_i l_j dr$ and $\left.\frac{dl_j}{dr}\right|_{r_i}$ can be precomputed and stored. Legendre-Gauss-Lobatto points has to be chosen as the interpolation points to minimize the computation error. For more details, we refer to Chapter 3 of reference [16]. For the time integration, a second order A-B scheme was also applied as discussed in Section (3.5).

The scheme previously presented can treat a hyperbolic problem. But in this setting Crank-Nicolson method is hard to apply, because the values at the interfaces are duplicated. We chose the problem formulation of Eq. (6), where the flux contains convective part F_c and viscous part F_v. For the convective part, Godunov flux is applicable. For the viscous flux, a straight idea is to use the central flux, $(F_v(U_L) + F_v(U_R))/2$. But as pointed out by Shu el al. [41], this choice is inconsistent.

To solve this problem, we rewrite the original equations as

$$\frac{\partial U}{\partial t} + \frac{\partial F_c}{\partial x} - C_v \frac{\partial q}{\partial x} = S$$
$$q - \frac{\partial Q}{\partial x} = 0$$

The semidiscrete form of the equation is

$$\frac{dU_k}{dt} = -\mathcal{D}^k F^k - (\mathcal{M}^k)^{-1}(-F^k l^k + F^* l^k)\Big|_{x_k}^{x_{k+1}} + S^k.$$
$$q^k = \mathcal{D}^k Q^k - (\mathcal{M}^k)^{-1}(-Q^k l^k + Q^* l^k)\Big|_{x_k}^{x_{k+1}}$$

The flux in these equations have to be modified accordingly: $F^k = F_c^k - C_v q^k$, $F^* = F_c^* - (C_v q)^*$. F_c^* is defined by Godunov flux. The numerical flux $(C_v q)^*$ and Q^* are defined by the central flux. The introduction of an auxiliary variable q stabilizes the scheme. Note that q^k can be eliminated in every time step, thus the addition of storage or computational cost is very limited. This method is called local Discontinuous Galerkin scheme.

4 Results and discussion

In this part, we first impose a small perturbation of the system and analyze several important behaviours of the wave: propagation, attenuation, diffusion, wavefront steepening, reflection and transmission at a branching point. Then we assume a larger perturbation and observe the forming of a shock. All of the schemes are tested on capturing these behaviours. Finally all of the schemes are applied on a relatively realistic network. In this setting, the performance of the schemes are compared.

4.1 Propagation in an uniform tube

In this subsection we compare the numerical results with analytical results on a single vessel for a pulse. The tube is long enough to avoid reflections. Adding a small perturbation $((\epsilon\tilde{A}, \epsilon\tilde{Q}))$ to the equilibrium solution $(U = (A_0, 0))$ of the governing equations, substituting and dropping the terms with quadratics of ϵ, assuming constant properties for artery $(\partial(\beta\sqrt{A_0})/\partial x = \partial\beta/\partial x = 0)$, gives the equations for the perturbations in a linear form:

$$\frac{\partial \tilde{A}}{\partial t} + \frac{\partial \tilde{Q}}{\partial x} = 0, \quad \frac{\partial \tilde{Q}}{\partial t} + c_0^2 \frac{\partial \tilde{A}}{\partial x} = -\frac{C_f}{A_0}\tilde{Q} + C_v \frac{\partial^2 \tilde{Q}}{\partial x^2} \tag{42}$$

with $c_0 = \sqrt{\frac{\beta}{2\rho}\sqrt{A_0}}$, the Moens-Korteweg celerity. We investigate the convection phenomena at first, so we drop the non-homogeneous part (no viscosities $C_f = 0$ and $C_v = 0$), Eq. (42) is the d'Alembert equation and admits the wave

solution. If we assume that the initial condition is $A = A_0, Q = 0$, and the inflow is prescribed as $Q(0,t) = Q_{in}(t)$ with

$$Q_{in}(t) = Q_c sin(\frac{2\pi}{T_c}t)H(-t + \frac{T_c}{2}), \quad t > 0,$$

with $H(t)$ the Heaviside function, then the solution is $c_0\tilde{A} = \tilde{Q} = Q_{in}(x - c_0 t)$, which means that the waveform propagates to the right with a speed of c_0.

We propose a numerical test with parameters of the tube inspired by [39]: $L = 250$cm, $A_0 = 3.2168\text{cm}^2$, $\beta = 1.8734 \times 10^6$Pa/m and $\rho = 1.050 \times 10^3\text{kg/m}^3$, and accordingly, $c_0 = 400$cm/s. To impose a small perturbation, we choose $Q_c =$ 1ml/s and $T_c = 0.4$s. The change ratio of the radius is $\Delta R/R_0 = Q_0/(2A_0c_0) =$ 0.04%. We take the linearized analytical solution at time $t = 0.4s$ as reference to compute the errors of the numerical schemes. We see on figure 4(a) that all the scheme give the same result. To analyze more closely the solution, we define the 1-norm of the errors as

$$||E||_1 = \frac{1}{N}\sum_{i=1}^{N} |\frac{Q_{numerical} - Q_{analytical}}{Q_c}|,$$

and we will test the spatial ($\Delta x = \frac{L}{N}$) and temporal ($\Delta t = C_t \frac{L}{Nc_0}$) convergence. For the DG scheme, the time step formula is modified accordingly as $\Delta t = \frac{C_t}{\mathcal{P}} \frac{L}{Nc_0}$, with $\mathcal{P}$ the order of the polynomial.

From our numerical test, we have the following observations. All the proposed scheme converge (Figures 4(a) and 4(b)) but with different speeds of convergence.

Fixing $C_t = 0.1$, $||E||_1$ are computed for several schemes with different N. The log-log plot of $||E||_1$ against Δx can be seen in Figure (4(b)). One can see that all of the schemes converge with an order between 1 and 2 and the DG schemes converges faster. If we fix the mesh ($N_{TG} = N_{FV} = N_{FD} = 800, N_{DG-\mathcal{P}_1} = N_{DG-\mathcal{P}_2} = 100$) and increase (or decrease) the time steps, the error varies slightly for all of the schemes except FV (see Figure 4(c)). If $C_t > 0.6$ for Taylor-Galerkin, FV or MacCormack, the scheme becomes unstable. For the DG scheme, C_t can not be greater than 0.1. So, for the convergence of the time integration we have to choose a smaller time step than the value prescribed by the CFL condition for stabilization reasons. To compare the actual speed and accuracy of the four schemes, we set N and C_t such that the errors achieve the same order of magnitude (see Table (1) and Figure 4(d)).

Except the Taylor-Galerkin scheme, all of the schemes have the similar accuracy with very close running time. At this point of the paper, the Taylor-Galerkin scheme shows the worst accuracy and needs to run the longest time, we will see that in fact as the time integration of Taylor-Galerkin is more efficient than the others, this conclusion will change in the network case (Section 4.6).

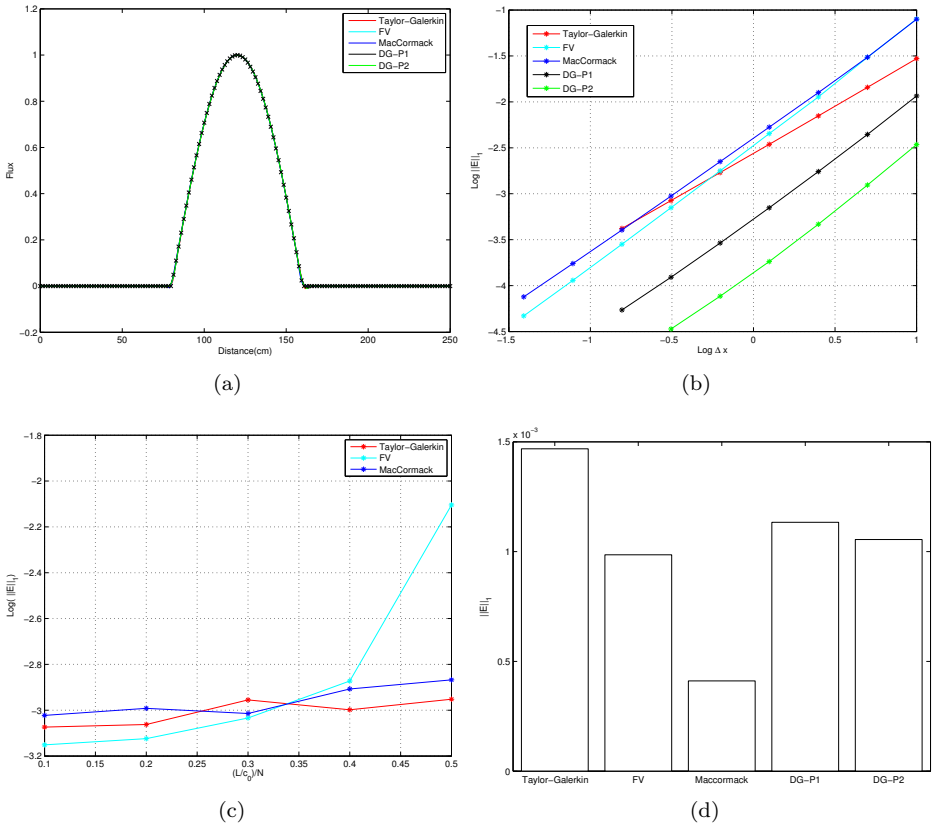

(a) (b) (c) (d)

Figure 4: Test on a uniform tube. Upper left, the pulse at time 0.4s, all the results are overlapped. Upper right, error of the schemes with different size of elements (cells). Lower left, at fixed mesh ($N_{TG} = N_{FV} = N_{FD} = 800$), error as a function of C_t coefficient. Lower right, a focus on the error for Table 1 values.

	N	C_t
Taylor-Gakerkin	800	0.5
FV	800	0.3
MacComack	1600	0.5
$DG - \mathcal{P}_1$	200	0.1
$DG - \mathcal{P}_2$	100	0.1

Table 1: Number of elements and coefficient of time step

4.2 Attenuation due to the viscosity of blood

We now consider the same linearized system (Eq. 42) with its small non-homogeneous viscous part ($C_f \neq 0$ and $C_v = 0$). The main dynamics of the system will be grossly the same traveling wave but attenuated by viscosity. This behaviour can be predicted by asymptotic analysis. We have a small non-dimensional parameter $\epsilon_f = T_c C_f / A_0$, which is the ratio of the characteristic time of pulse T_c to the characteristic time of attenuation A_0/C_f. In order to see how the waveform slowly evolves when it propagates to, say right, we make a change of variables to $\tau = \epsilon_f t$ and $\xi = x - c_0 t$ (slow time, moving frame). The two differential operators ∂_t and ∂_x expand as

$$\frac{\partial}{\partial t} = \frac{\partial \tau}{\partial t}\frac{\partial}{\partial \tau} + \frac{\partial \xi}{\partial t}\frac{\partial}{\partial \xi} = \epsilon_f \frac{\partial}{\partial \tau} - c_0 \frac{\partial}{\partial \xi}$$
$$\frac{\partial}{\partial x} = \frac{\partial \xi}{\partial x}\frac{\partial}{\partial \xi} = \frac{\partial}{\partial \xi}$$

The solution has the asymptotic expansion

$$\tilde{A} = \tilde{A}_0 + \epsilon_f \tilde{A}_1 + ... \quad \tilde{Q} = \tilde{Q}_0 + \epsilon_f \tilde{Q}_1 + ...$$

Substituting these into the governing equations expressed in new variables and collecting the terms with the same order of ϵ_f, one has

$$(-c_0 \frac{\partial \tilde{A}_0}{\partial \xi} + \frac{\partial \tilde{Q}_0}{\partial \xi}) + \epsilon_f (\frac{\partial \tilde{A}_0}{\partial \tau} - c_0 \frac{\partial \tilde{A}_1}{\partial \xi} + \frac{\partial \tilde{Q}_1}{\partial \xi}) + .. = 0$$
$$(-c_0 \frac{\partial \tilde{Q}_0}{\partial \xi} + c_0^2 \frac{\partial \tilde{A}_0}{\partial \xi}) + \epsilon_f (\frac{\partial \tilde{Q}_0}{\partial \tau} - c_0 \frac{\partial \tilde{Q}_1}{\partial \xi} + c_0^2 \frac{\partial \tilde{A}_1}{\partial \xi} + \frac{\tilde{Q}_0}{T_c}) + .. = 0$$

We take the first order term in ϵ_f in the first equation, we substitute it in the first order term in ϵ_f in the second equation, hence we obtain:

$$(\frac{\partial \tilde{Q}_0}{\partial \tau} + c_0 \frac{\partial \tilde{A}_0}{\partial \tau} + \frac{\tilde{Q}_0}{T_c}) = 0.$$

From terms of the zeroth order in ϵ_f, which involve derivative in ξ only, the solution must have the form $\tilde{Q}_0 = c_0 \tilde{A}_0(\tau, \xi) + \phi(\tau)$. The previous equation will

imply terms $\frac{\partial \phi}{\partial \tau}$ and $\phi(\tau)$ which are secular terms and so which are null. So $c_0 \tilde{A}_0 = \tilde{Q}_0$, thus we have $\frac{\partial \tilde{Q}_0}{\partial \tau} = -\frac{1}{2T_c}\tilde{Q}_0$, or

$$\tilde{Q}_0 = \tilde{Q}_0(0,\xi)e^{-\tau/(2T_c)} = \tilde{Q}_0(0, x - c_0 t)e^{-\epsilon_f t/(2T_c)}.$$

For more on asymptotic analysis of blood flow in large blood vessels, we refer to reference ([47]).

In Figure (5), we plot the snapshots of the waveform at time 0.2s, 0.4s, 0.6s and 0.8s. In the computation, the initial and boundary conditions are the same as in the previous subsection. The mesh and the time steps in Table (1) are adopted. The damping rate of the amplitude of the waveform agrees very well with the analytical prediction, $\exp(-\frac{C_f x}{2A_0 c_0})$, which is indicated by the dashed line. Also note that the errors of different schemes are not the same. The FV scheme causes the peak of the wave to slightly flatten, while all of the other schemes are dispersive: we have small oscillations at the foot of the signal.

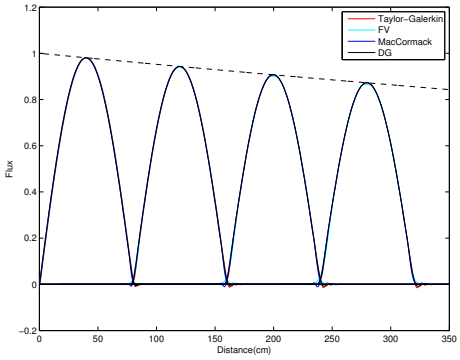

Figure 5: Attenuation due to the skin friction. The snapshots are at time 0.2s, 0.4s, 0.6s and 0.8s. The dashed line is $\exp(-\frac{C_f x}{2A_0 c_0})$ with $2A_0 c_0/C_f \simeq 2000$cm The flux is normalized with respect to Q_c

4.3 Diffusion due to the viscosity of the arterial wall

We now consider the same linearized system (Eq. 42) but with now the Kelvin-Voigt effect and no viscous fluid effect ($C_f = 0$ and $C_v \neq 0$). The small parameter is now $\epsilon_v = C_v/(c_0^2 T_c)$. If we apply the same technique as described in the previous subsection, we can readily obtain the diffusive behaviour of the pulse in the moving frame:

$$\frac{\partial \tilde{Q}_0}{\partial \tau} = \frac{c_0^2 T_c}{2}\frac{\partial^2 \tilde{Q}_0}{\partial^2 \xi} \tag{43}$$

The solution of this equation can be given by the convolution

$$\tilde{Q}_0(\tau,\xi) = \int_{-\infty}^{+\infty} \tilde{Q}_0(0,\xi)G(\tau, \xi - \zeta)d\zeta$$

where G is the fundamental solution of the heat equation (43)

$$G(\tau, \xi) = \frac{1}{\sqrt{2\pi\tau c_0^2 T_c}} e^{-\xi^2/(2\tau c_0^2 T_c)}$$

In the test vessel, the parameters are kept the same as in the case of attenuation. The coefficient C_v is 0.6275 m^2/s and $\epsilon_v \simeq 0.1$. This corresponds to $\phi = 5000Pa \cdot s$, which is in the range of observed values on animals [2]. To facilitate the calculation of the analytical solution, non-reflecting B.C. are imposed at the two ends of the vessel and I.C. is a half sinusoidal waveform for flux Q and a constant cross section A_0, see Figure (6). It is clear that half of the initial wave propagates to right and at the same time the waveform is spread out due to the diffusive effect. The analytical solution at time 0.4s (indicated by crossing signs) agrees very well with all of the numerical solutions.

Another point worthy noticing is the operator splitting errors. In the DG scheme, no operator splitting error is induced. All of the other numerical schemes where operator splitting method. It produces very accurate solutions as well as DG. Thus, it verifies the *a priori* judgement that Godunov splitting is sufficient.

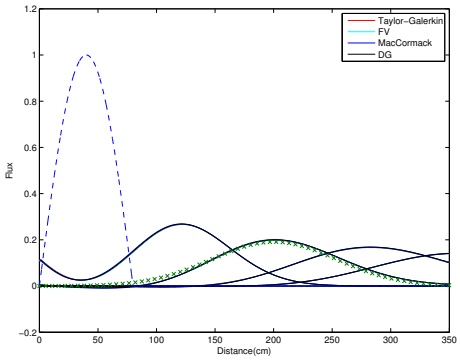

Figure 6: Diffusion due to the viscosity of the wall. The dashed line is the initial condition. One half of the original waveform propagates to right. The snap shots are at time 0.2s, 0.4s, 0.6s and 0.8s. The analytical prediction from the convolution at time 0.4s is indicated by crossing signs. The difference between the different numerical solutions is not discernible. The flux is normalized with respect to Q_c.

4.4 Wavefront steepening due to the nonlinearity

We now consider the full nonlinear system , but without Kelvin-Voigt effect and no viscous fluid effect ($C_f = 0$ and $C_v = 0$). The small parameter is now $\epsilon_2 = Q_c/(c_0 A_0)$. If we apply the same technique as described in the previous subsection, we can readily obtain the non linear behaviour of the pulse in the

moving frame (inviscid Burgers equation):

$$\frac{\partial \tilde{Q}_0}{\partial \tau} = \frac{1}{2A_0}\tilde{Q}_0 \frac{\partial \tilde{Q}_0}{\partial \xi} \tag{44}$$

One important consequence of nonlinear hyperbolic system that shocks may arise even if the initial condition is very smooth. In normal physiological conditions, shocks are not observed in arterial systems. But in venous system, shock-like phenomena may occur on muscular veins during walking and running. The intramuscular pressure (equivalent to P_{ext} in our model) can rise to $20 - 40kPa$ in few ms [3]. In such situation, experiment and numerical simulations [9, 27] have shown this critical behaviour. For another example, the traumatic rupture of the aorta is responsible for a significant percentage of traffic death and the rupture may be well accounted by the the shock-like transition resulted from the blunt impact to the thorax [18]. Thus we test all of the schemes in such case. To observe a shock, only two parameters are modified: $L = 800$cm and $Q_c = 200$ml/s. The change ratio of the radius is about 7.78 %. The number of elements for Taylor-Galerkin, FV and MacComack schemes is 800. The DG scheme uses 200 elements and the order of polynomial is 2. Figure (7) shows that a shock starts to form around the point 300cm. Strong oscillations are generated at the front foot of the waveform by Taylor-Galerkin scheme. On the other hand, strong oscillations are induced at the back of the great gradients. For the DG scheme, there are some smaller oscillations both in front and back. That is because the characteristic structures are taken into account in the numerical flux. Limiters may be introduced to eliminate the oscillations. This remedy will be necessary for DG to be applicable on problems with shocks. For the FV scheme, the shock is well captured without nonphysical oscillations. That verifies the total-variation-diminishing (TVD) property of the FV scheme.

On Figure (7(b)) we plot a case with some viscosity in the wall. The small added diffusion smoothes the oscillations and all of the schemes give almost the same result with moderate diffusion.

4.5 Reflection and transmission at a branching point

Up to now, we focus on the various physical terms in the equations, propagation, attenuation, non linearities... Now, we look at the boundaries or each artery. Indeed, pressure waves are reflected and transmitted at the conjunction points of the arteries. For linearized models, the reflection and transmission coefficients at a branching are given by the formula [14, 33] in terms of Z defined as $Z = \frac{\rho c_0}{A_0}$ the impedance:

$$\mathcal{R} = \frac{Z_p^{-1} - (Z_{d_1}^{-1} + Z_{d_2}^{-1})}{Z_p^{-1} + (Z_{d_1}^{-1} + Z_{d_2}^{-1})}, \quad \mathcal{T} = \frac{2Z_p^{-1}}{Z_p^{-1} + (Z_{d_1}^{-1} + Z_{d_2}^{-1})},$$

where Z_p and Z_d are the characteristic impedance of the parent and daughter vessels. In Figure (8), for sake of illustration, the configuration of the branching

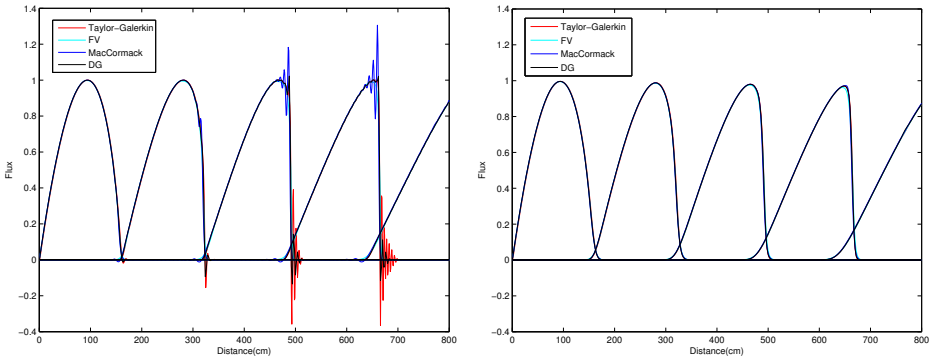

(a) (b)

Figure 7: Shock due to the convective term. The left figure (a) shows that sharp gradient forms in a nonlinear hyperbolic system. Numerical schemes may cause spurious oscillations. FV scheme with a flux limiter captures the shock without non-physical oscillations. The right figure (b) shows that all of the schemes give almost the same result for a system with a moderate diffusion term.

and the time profile of pressure at two locations are shown. The amplitude is normalized with respect to $Q_c = 1 \times 10^{-6}\text{m}^3/\text{s} = 1\text{ml/s}$. For the parent vessels: $\beta = 2.3633 \times 10^6 Pa/m$, $A_0 = 4\text{cm}^2$ and for each of the daughter vessels: $\beta = 6.3021 \times 10^6\text{Pa/m}$, $A_0 = 1.5\text{cm}^2$. According to the formula, $\mathcal{R} = 0.2603$ and $\mathcal{T} = 1.2603$. The pressure waveform at the points A and B agrees very well with analytical prediction. All of the numerical schemes are compatible with this treatment of conjunction.

4.6 Application on a full systematic arterial system

As already mentioned in the introduction, a relatively realistic description of arterial system has been done by 1D simulations, with different numerical solvers in different teams. For example, in [30, 39], Galerkin approach was used. In these papers, wall viscosity is not included. We include the diffusive term and present the numerical treatment of this term. In other literatures [42, 37], finite difference schemes are adopted. Note that [37] gives a survey of the literature on the subject. But, the numerical errors and the running time are not known compared with other numerical schemes in all those paper. In this paper, we will compare the running time and the results of all the methods. To do this, the structure and stiffness of the arterial network are adapted from [39]. The viscosity coefficient of the Kelvin-Voigt model on human body is not known. To propose some realistic values, we follow reference [2] where the viscosity of aortic wall of dogs was modeled by a Kelvin-Voigt model and the value of ϕ was in the range $3.8 \pm 1.3 \times 10^3 Pa \cdot s$ to $7.8 \pm 1.1 \times 10^3 Pa \cdot s$. Hence, we assume $\phi = 5 \times 10^3 Pa \cdot s$ and calculate ν_s by formula 4 and further calculate C_v by

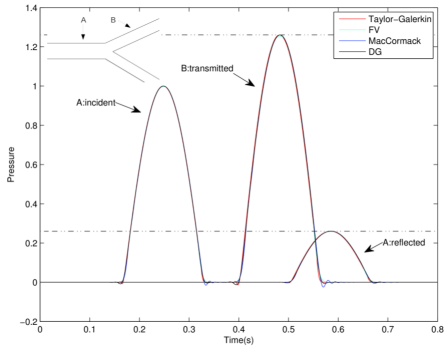

Figure 8: Reflection and transmission of pressure wave at a branching point. The time profiles of the pressure at points A and B are plotted. The analytical reflection and transmission coefficients are 0.2603 and 1.2603 (indicated by the dashed line).

$C_v = \frac{A_0 \nu_s}{\rho}$. The final parameters of the network we use are shown in Table 3. We note that there may be differences between arteries in human and dog and the arteries in different locations may cause a considerable variation. Nevertheless the inclusion of viscosity term make it possible to test the numerical schemes in a more realistic condition.

The peak value of the input flux Q_c is 500 ml/s. This value is very close to the peak flow rate at the root of aortic artery [37]. We choose $\min_{i=1}^{i=55}(L^i/c_0^i)$ as a reference element length, with L^i the length of the i-th artery and c_0^i the wave speed of the linearized system. For a coarsest possible mesh, the number of elements (cells) of each artery is $N_{base}^i = \lfloor \frac{L^i}{\min_{i=1}^{i=55}(L^i/c_0^i)} \rfloor$, where $\lfloor \cdot \rfloor$ is floor function. We computed the relative change of solutions when the number of the elements (cells) are doubled. Figure (9) shows the relative change of the solutions when the number of the elements (cells) is changed from $2N_{base}$ to $4N_{base}$. The relative change of a quantity (for example flux Q) with two meshes N_1 and N_2 is defined as $||Q_{N_1} - Q_{N_2}||_1/(Q_{max} - Q_{min})$, where $||\cdot||_1$ stands for 1-norm, Q_{max} and Q_{min} are the maximum and minimum values within one heart beat. Figure (9) shows that the change of flux and pressure are less than 1.5% for all of of the schemes except DG. Thus we plotted in Figure (10) the results computed with mesh $2N_{base}$.

The DG scheme is not tested in this manner because it is already converged: result in Figure (10) shows that the error for DG is already very small with the coarsest possible mesh.

Time step is $\Delta t = C_t \min_{i=1}^{i=55}(\frac{L^i}{N^i c_0})$. The coefficient of C_t and the corresponding real time step is shown in Table (2)

In Figure (10) we plot the history profile of flux and pressure at the middle of four representative arteries. All of the numerical solutions agree very well. The main following qualitative behaviours reported in literature [39, 37] are ob-

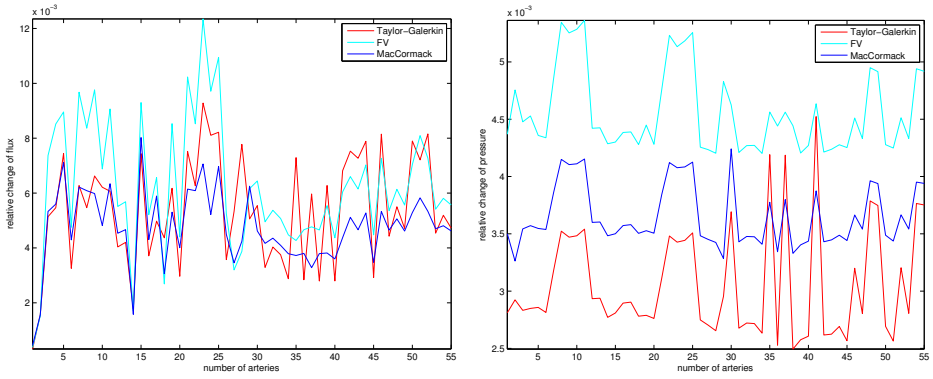

(a) (b)

Figure 9: Relative change of the solutions when the mesh is doubled from $2N_{base}$ to $4N_{base}$. The left figure shows that the relative error of all of the flux is less than 1.3 %. The right figure shows that the relative change of all of the pressure is less then 0.6% .

	C_t	$\Delta t(10^{-6}s)$	running time for one heart beat (minutes)
Taylor-Gakerkin	0.4	222	22.0
FV	0.25	139	31.9
MacComack	0.1	55.5	91.2
DG	0.006	6.66	576

Table 2: Time steps and running time in minutes on a standard Linux Work Station for all of the schemes

served. The peak value of pressure waveform increases as we travel down the system. We can also see the dicrotic notch at artery 1. At artery 37, a reverse flow is observed, see 10(f). This phenomena is also observed in clinical measurement [37]. The result in this paper is smoother than the corresponding arteries in [39]. The result with viscosities is closer to the clinical observations [37]. We realize that it is very important to consider the wall viscosities to give more realistic result. This agrees with the conclusion drawn by the comparison of numerical results with data from *in vitro* experiments [1, 38].

5 Conclusions

In this paper, we presented four numerical schemes for a 1D viscoelastic blood flow model. Under the assumptions of small nonlinearities, analytical solutions predict several behaviours of the wave: propagation in a uniform tube, attenuation of the amplitude due to the skin friction, and diffusion due to the viscosity of the wall (note that the effect of dispersion will be examined in the future). These

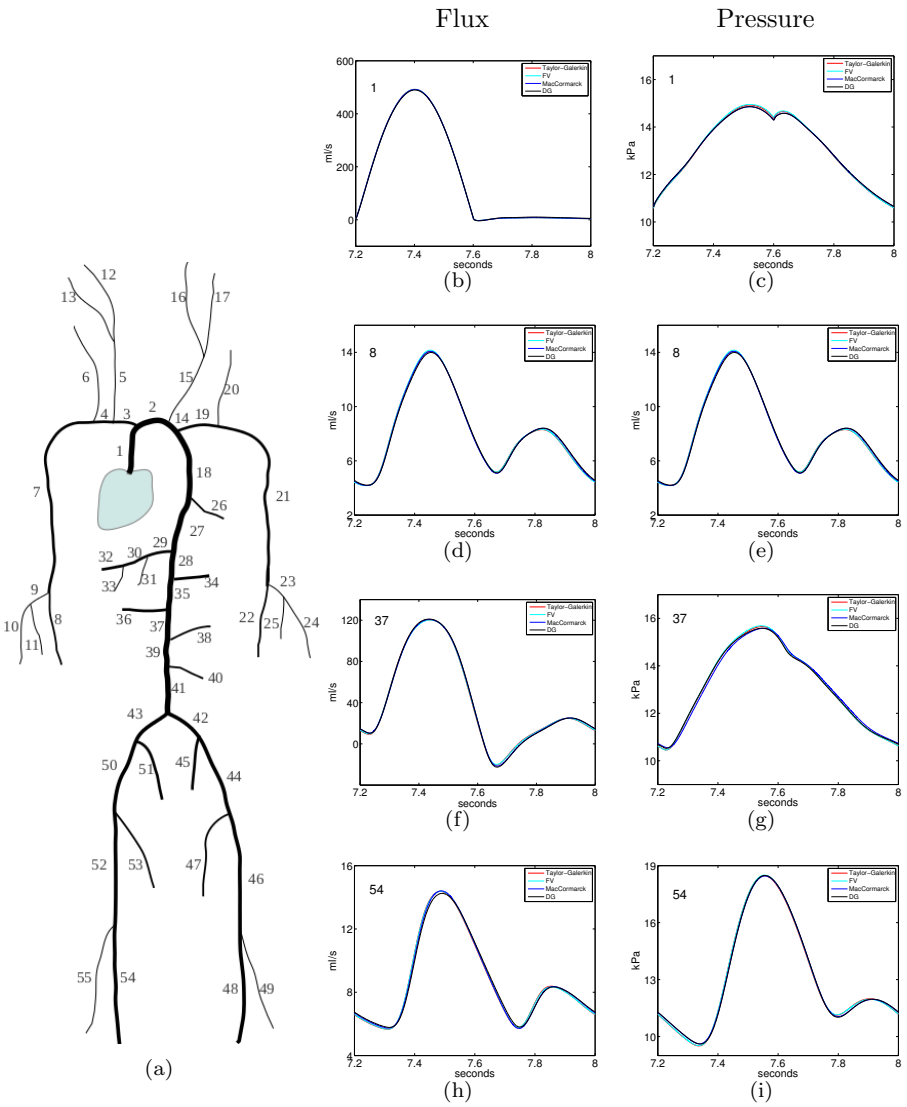

Figure 10: The history profiles of pressure and flux at four locations. Ten heart beats are computed to secure steady state is achieved and the tenth heart beat is plotted. The differences between the four numerical schemes are very small.

predictions were compared with all of the numerical solutions. After that, we applied all of the schemes on a relatively realistic arterial system. The schemes can be compared in three aspects: the accuracy, the ability to capture shock phenomena, the computation speed and the complexity of the implementation.

1. MacCormack and Taylor-Galerkin schemes generate small oscillations. FV scheme has slight arbitrary steepening effect. Both diffusion and dispersion errors are very small for DG. Nevertheless all of the schemes converge with a moderate fine mesh and precisely capture the various phenomena of this hyperbolicity dominating hyperbolic-parabolic system.

2. MacCormack and Taylor-Galerkin perform very poorly when there is a steep gradient. Both of them present strong oscillations at one side of the jumping location. DG scheme has smaller oscillations at both sides of the jump. Numerical flux limiters are possible to filter out the oscillations. That will further complicate the schemes and the theory and technique is still under research [19, 27]. On the other hand, there are very mature techniques to impose a slope limiter in the FV scheme. Shock capturing property is unique for FV among the four schemes presented in this paper.

3. For a network of human size, the speed of computation can be ordered from fast to slow as: Taylor-Galerkin, second order FV, MacCormack and DG. The time integration in the Taylor-Galerkin scheme is more efficient than Adams-Bashforth 2-step method. Thus it allows a larger time step with a comparable accuracy. But if the number of elements for one artery is too large (larger than 500), the speed of Taylor-Galerkin becomes slower because the size of the global matrix increases quadratically and thus the storing and inverting of matrix becomes very expansive. The DG scheme prevents the application of Crank-Nicolson method on the diffusion term. An explicit method called local DG scheme was adopted in this paper. Even with a moderate diffusion coefficient (within the range observed in physiological condition), a very small time step is necessary for stability. That makes the computation of 1 heart beat cost about 9 hours while all of the other schemes cost only 20 to 90 minutes (on a standard Linux Work Station).

4. From easiest to hardest, the implementation of the schemes can be ordered: MacCormack, second order FV, Taylor-Galerkin and local DG.

As a final conclusion from the point of view of practical application, we recommend MacCormack in case of very small nonlinearities; second order FV will be a very good option if there maybe shock-like phenomena in the systems; Taylor-Galerkin has quite balanced properties between speed and accuracy if no shock-like phenomena may present in the system; DG is suitable for systems with very small physical diffusion term since both the numerical diffusion and dispersion are very small in this scheme.

Acknowledgements

The first author would like to thank the partial financial aid of China Scholarship Council. We wish to gratefully thank Jean-Frédéric Gerbeau for helpful discussion and implementation of the Taylor-Galerkin scheme, and Olivier Delestre for finite volume scheme.

References

[1] J. Alastruey, A.W. Khir, K.S. Matthys, P. Segers, S.J. Sherwin, P.R. Verdonck, K.H. Parker, and J. Peiró. Pulse wave propagation in a model human arterial network: Assessment of 1-d visco-elastic simulations against *in vitro* measurements. *Journal of Biomechanics*, 2011.

[2] R.L. Armentano, J.G. Barra, J. Levenson, A. Simon, and R.H. Pichel. Arterial wall mechanics in conscious dogs: assessment of viscous, inertial, and elastic moduli to characterize aortic wall behavior. *Circulation Research*, 76(3):468–478, 1995.

[3] R.E. Ballard, D.E. Watenpaugh, G.A. Breit, G. Murthy, D.C. Holley, and A.R. Hargens. Leg intramuscular pressures during locomotion in humans. *Journal of Applied Physiology*, 84(6):1976–1981, 1998.

[4] Cristobal Bertoglio, Philippe Moireau, and Jean-Frederic Gerbeau. Sequential parameter estimation for fluid–structure problems: Application to hemodynamics. *International Journal for Numerical Methods in Biomedical Engineering*, 2012.

[5] J. Blacher, R. Asmar, S. Djane, G.M. London, and M.E. Safar. Aortic pulse wave velocity as a marker of cardiovascular risk in hypertensive patients. *Hypertension*, 33(5):1111–1117, 1999.

[6] N. Cavallini, V. Caleffi, and V. Coscia. Finite volume and weno scheme in one-dimensional vascular system modelling. *Computers and Mathematics with Applications*, 56(9):2382–2397, 2008.

[7] O. Delestre, P.Y. Lagrée, et al. A well balanced finite volume scheme for blood flow simulation. *International Journal for Numerical Methods in Fluids*, page doi: 10.1002/fld.3736, 2012.

[8] D. Elad, D. Katz, E. Kimmel, and S. Einav. Numerical schemes for unsteady fluid flow through collapsible tubes. *Journal of Biomechanical Engineering*, 13(1):10–18, 1991.

[9] P. Flaud, P. Guesdon, and J.M. Fullana. Experiments of draining and filling processes in a collapsible tube at high external pressure. *The European Physical Journal Applied Physics*, 57(03), 2012.

[10] L. Formaggia, J.F. Gerbeau, F. Nobile, and A. Quarteroni. On the coupling of 3d and 1d navier–stokes equations for flow problems in compliant vessels. *Computer Methods in Applied Mechanics and Engineering*, 191(6):561–582, 2001.

[11] L. Formaggia, D. Lamponi, and A. Quarteroni. One-dimensional models for blood flow in arteries. *Journal of Engineering Mathematics*, 47(3):251–276, 2003.

[12] L. Formaggia, A. Quarteroni, and A. Veneziani. *Cardiovascular Mathematics: Modeling and simulation of the circulatory system*, volume 1. Springer, 2009.

[13] J.M. Fullana and S. Zaleski. A branched one-dimensional model of vessel networks. *Journal of Fluid Mechanics*, 621(1):183–204, 2009.

[14] Y. Fung. *Biomechanics: circulation*. Springer Verlag, 1997.

[15] Jean-Frédéric Gerbeau, Marina Vidrascu, and Pascal Frey. Fluid–structure interaction in blood flows on geometries based on medical imaging. *Computers and Structures*, 83(2):155–165, 2005.

[16] J.S. Hesthaven and T. Warburton. *Nodal discontinuous Galerkin methods: algorithms, analysis, and applications*, volume 54. Springer-Verlag New York Inc, 2008.

[17] E. Kimmel, RD Kamm, AH Shapiro, et al. Numerical solutions for steady and unsteady flow in a model of the pulmonary airways. *Journal of Biomechanical Engineering*, 110(4):292, 1988.

[18] Y. Kivity and R. Collins. Nonlinear wave propagation in viscoelastic tubes: application to aortic rupture. *Journal of Biomechanics*, 7(1):67–76, 1974.

[19] Dmitri Kuzmin. Slope limiting for discontinuous galerkin approximations with a possibly non-orthogonal taylor basis. *International Journal for Numerical Methods in Fluids*, 2012.

[20] Pierre-Yves Lagrée and Maurice Rossi. Etude de l'écoulement du sang dans les artères: effets nonlinéaires et dissipatifs. *Comptes Rendus de l'Academie des Sciences-Serie IIb-Mecanique Physique Chimie Astronomie*, 322(5):401–408, 1996.

[21] P.Y. Lagrée. An inverse technique to deduce the elasticity of a large artery. *EPJ Applied Physics*, 9(2):153–164, 2000.

[22] R.J. LeVeque. *Finite volume methods for hyperbolic problems*, volume 31. Cambridge University Press, 2002.

[23] J. Lighthill. *Waves in fluids*. Cambridge University Press, 2001.

[24] R.W. MacCormack. The effect of viscosity in hypervelocity impact cratering. *Frontiers of Computational Fluid Dynamics*, pages 27–44, 1969.

[25] A Cristiano I Malossi, Pablo J Blanco, and Simone Deparis. A two-level time step technique for the partitioned solution of one-dimensional arterial networks. *Computer Methods in Applied Mechanics and Engineering*, 2012.

[26] G. Mancia, G. De Backer, A. Dominiczak, R. Cifkova, R. Fagard, G. Germano, G. Grassi, A.M. Heagerty, S.E. Kjeldsen, S. Laurent, et al. 2007 guidelines for the management of arterial hypertension the task force for the management of arterial hypertension of the european society of hypertension (esh) and of the european society of cardiology (esc). *European Heart Journal*, 28(12):1462–1536, 2007.

[27] Emilie Marchandise and Patrice Flaud. Accurate modelling of unsteady flows in collapsible tubes. *Computer Methods in Biomechanics and Biomedical Engineering*, 13(2):279–290, 2010.

[28] Emilie Marchandise, Marie Willemet, and Valérie Lacroix. A numerical hemodynamic tool for predictive vascular surgery. *Medical Engineering and Physics*, 31(1):131–144, 2009.

[29] K.S. Matthys, J. Alastruey, J. Peiró, A.W. Khir, P. Segers, P.R. Verdonck, K.H. Parker, and S.J. Sherwin. Pulse wave propagation in a model human arterial network: Assessment of 1-d numerical simulations against *in vitro* measurements. *Journal of Biomechanics*, 40(15):3476–3486, 2007.

[30] J.P. Mynard and P. Nithiarasu. A 1d arterial blood flow model incorporating ventricular pressure, aortic valve and regional coronary flow using the locally conservative galerkin (lcg) method. *Communications in Numerical Methods in Engineering*, 24(5):367–417, 2008.

[31] F. Nicoud, H. Vernhet, and M. Dauzat. A numerical assessment of wall shear stress changes after endovascular stenting. *Journal of Biomechanics*, 38(10):2019–2027, 2005.

[32] M.S. Olufsen, C.S. Peskin, W.Y. Kim, E.M. Pedersen, A. Nadim, and J. Larsen. Numerical simulation and experimental validation of blood flow in arteries with structured-tree outflow conditions. *Annals of Biomedical Engineering*, 28(11):1281–1299, 2000.

[33] T.J. Pedley. *The Fluid Mechanics of Large Blood Vessels*. Cambridge University Press, 1980.

[34] A.J. Pullan, N.P. Smith, and P.J. Hunter. An anatomically based model of transient coronary blood flow in the heart. *SIAM Journal on Applied mathematics*, 62(3):990–1018, 2002.

[35] Rashmi Raghu, Irene E Vignon-Clementel, C Alberto Figueroa, Charles A Taylor, et al. Comparative study of viscoelastic arterial wall models in nonlinear one-dimensional finite element simulations of blood flow. *Journal of biomechanical engineering*, 133(8):081003, 2011.

[36] P. Reymond, Y. Bohraus, F. Perren, F. Lazeyras, and N. Stergiopulos. Validation of a patient-specific one-dimensional model of the systemic arterial tree. *American Journal of Physiology-Heart and Circulatory Physiology*, 301(3):H1173–H1182, 2011.

[37] P. Reymond, F. Merenda, F. Perren, D. Rüfenacht, and N. Stergiopulos. Validation of a one-dimensional model of the systemic arterial tree. *American Journal of Physiology-Heart and Circulatory Physiology*, 297(1):H208–H222, 2009.

[38] M. Saito, Y. Ikenaga, M. Matsukawa, Y. Watanabe, T. Asada, and P.Y. Lagrée. One-dimensional model for propagation of a pressure wave in a model of the human arterial network: Comparison of theoretical and experimental results. *Journal of Biomechanical Engineering*, 133:121005, 2011.

[39] S.J. Sherwin, L. Formaggia, J. Peiro, and V. Franke. Computational modelling of 1d blood flow with variable mechanical properties and its application to the simulation of wave propagation in the human arterial system. *International Journal for Numerical Methods in Fluids*, 43(6-7):673–700, 2003.

[40] S.J. Sherwin, V. Franke, J. Peiró, and K. Parker. One-dimensional modelling of a vascular network in space-time variables. *Journal of Engineering Mathematics*, 47(3):217–250, 2003.

[41] C.W. Shu et al. Different formulations of the discontinuous galerkin method for the viscous terms. *Advances in Scientific Computing*, pages 144–155, 2001.

[42] N. Stergiopulos, D.F. Young, and T.R. Rogge. Computer simulation of arterial flow with applications to arterial and aortic stenoses. *Journal of Biomechanics*, 25(12):1477–1488, 1992.

[43] J. Wan, B. Steele, S.A. Spicer, S. Strohband, G.R. Feijo, T.J.R. Hughes, and C.A. Taylor. A one-dimensional finite element method for simulation-based medical planning for cardiovascular disease. *Computer Methods in Biomechanics and Biomedical Engineering*, 5(3):195–206, 2002.

[44] J.J. Wang and K.H. Parker. Wave propagation in a model of the arterial circulation. *Journal of Biomechanics*, 37(4):457–470, 2004.

[45] X. Wang, O Delestre, J-M Fullana, M Saito, Y Ikenaga, M Matsukawa, and P-Y Lagree. Comparing different numerical methods for solving arterial 1d flows in networks. *Computer Methods in Biomechanics and Biomedical Engineering*, 15(sup1):61–62, 2012.

[46] Micheal Wibmer. *One-dimensional simulation of arterial blood flow with applications*. PhD thesis, Vienna University of Technology, 2004.

[47] Sigeo Yomosa. Solitary waves in large blood vessels. *Journal of the Physical Society of Japan*, 56:506–520, 1987.

[48] Mokhtar Zagzoule and Jean-Pierre Marc-Vergnes. A global mathematical model of the cerebral circulation in man. *Journal of Biomechanics*, 19(12):1015–1022, 1986.

Table 3: Arterial network

ID	Name	l (cm)	A_0 (cm^2)	β (10^6Pa/cm)	C_v ($10^4cm^2/s$)	R_t
1	Ascending aorta	4.0	6.789	0.023	0.352	–
2	Aortic arch I	2.0	5.011	0.024	0.317	–
3	Brachiocephalic	3.4	1.535	0.049	0.363	–
4	R.subclavian I	3.4	0.919	0.069	0.393	–
5	R.carotid	17.7	0.703	0.085	0.423	–
6	R.vertebral	14.8	0.181	0.470	0.595	0.906
7	R. subclavian II	42.2	0.833	0.076	0.413	–
8	R.radius	23.5	0.423	0.192	0.372	0.82
9	R.ulnar I	6.7	0.648	0.134	0.322	–
10	R.interosseous	7.9	0.118	0.895	0.458	0.956
11	R.ulnar II	17.1	0.589	0.148	0.337	0.893
12	R.int.carotid	17.6	0.458	0.186	0.374	0.784
13	R. ext. carotid	17.7	0.458	0.173	0.349	0.79
14	Aortic arch II	3.9	4.486	0.024	0.306	–
15	L. carotid	20.8	0.536	0.111	0.484	–
16	L. int. carotid	17.6	0.350	0.243	0.428	0.784
17	L. ext. carotid	17.7	0.350	0.227	0.399	0.791
18	Thoracic aorta I	5.2	3.941	0.026	0.312	–
19	L. subclavian I	3.4	0.706	0.088	0.442	–
20	L. vertebral	14.8	0.129	0.657	0.704	0.906
21	L. subclavian II	42.2	0.650	0.097	0.467	–
22	L. radius	23.5	0.330	0.247	0.421	0.821
23	L. ulnar I	6.7	0.505	0.172	0.364	–
24	L. interosseous	7.9	0.093	1.139	0.517	0.956
25	L. ulnar II	17.1	0.461	0.189	0.381	0.893
26	intercoastals	8.0	0.316	0.147	0.491	0.627
27	Thoracic aorta II	10.4	3.604	0.026	0.296	–
28	Abdominal aorta I	5.3	2.659	0.032	0.311	–
29	Celiac I	2.0	1.086	0.056	0.346	–
30	Celiac II	1.0	0.126	0.481	1.016	–
31	Hepatic	6.6	0.659	0.070	0.340	0.925
32	Gastric	7.1	0.442	0.096	0.381	0.921
33	Splenic	6.3	0.468	0.109	0.444	0.93
34	Sup. mensenteric	5.9	0.782	0.083	0.439	0.934
35	Abdominal aorta II	1.0	2.233	0.034	0.301	–
36	L. renal	3.2	0.385	0.130	0.481	0.861
37	Abdominal aorta III	1.0	1.981	0.038	0.320	–
38	R. renal	3.2	0.385	0.130	0.481	0.861
39	Abdominal aorta IV	10.6	1.389	0.051	0.358	–
40	Inf. mesenteric	5.0	0.118	0.344	0.704	0.918
41	Abdominal aorta V	1.0	1.251	0.049	0.327	–
42	R. com. iliac	5.9	0.694	0.082	0.405	–
43	L. com. iliac	5.8	0.694	0.082	0.405	–
44	L. ext. iliac	14.4	0.730	0.137	0.349	–
45	L. int. iliac	5.0	0.285	0.531	0.422	0.925
46	L. femoral	44.3	0.409	0.231	0.440	–
47	L. deep femoral	12.6	0.398	0.223	0.419	0.885
48	L. post. tibial	32.1	0.444	0.383	0.380	0.724
49	L. ant. tibial	34.3	0.123	1.197	0.625	0.716
50	L. ext. iliac	14.5	0.730	0.137	0.349	–
51	R. int. iliac	5.0	0.285	0.531	0.422	0.925
52	R. femoral	44.4	0.409	0.231	0.440	–
53	R. deep femoral	12.7	0.398	0.223	0.419	0.888
54	R. post. tibial	32.2	0.442	0.385	0.381	0.724
55	R. ant. tibial	34.4	0.122	1.210	0.628	0.716

Data adapted from [39] and [2].